Seismic characterization of multiple fracture sets from multicomponent, multiazimuth, 3D data: Rulison Field, CO

Ivan Vasconcelos[†] and Vladimir Grechka[⋆]

[†] *Department of Geophysics, Colorado School of Mines, Golden, CO 80401, USA*

[⋆] *Shell International Exploration and Production, Inc., 3737 Bellaire Blvd., P. O. Box 481, Houston, TX, 77001-0481, USA*

ABSTRACT

Conventional fracture-characterization methods assume the presence of a single set of aligned, vertical cracks in the subsurface. We relax this assumption and demonstrate the feasibility of seismic characterization of *multiple* fracture sets. Our technique relies on recent theoretical findings indicating that multiple, differently oriented, possibly intersecting planar cracks embedded in an otherwise isotropic host rock result in an approximately orthotropic effective media. Here, the governing parameters of crack-induced orthotropy are estimated from 3D, wide-azimuth, multicomponent (P-, fast shear-, and slow shear-wave) seismic reflection data acquired over the tight-gas Rulison Field in Colorado.

We use strong azimuthal variations of the normal-moveout velocities to invert for the interval crack densities, fracture orientations, type of fluid infill, and velocities of P- and S-waves in the unfractured rock. Our inversion procedure identifies a set of cracks approximately aligned in the WNW-ESE direction in the western part of the study area and multiple, likely intersecting fractures in its eastern part. We validate both our underlying theoretical model and the obtained estimates by a number of independent measurements: (i) the estimated fluid-infill parameter indicates dry cracks as expected for the gas-producing sandstones at Rulison; (ii) our model predicts almost elliptical anisotropy and, indeed, the long-spread P-wave data exhibit no nonhyperbolic moveout; (iii) the obtained crack orientations are supported by well observations. As a by-product of fracture characterization, we build an anisotropic velocity model of the Rulison reservoir which, we believe, is the first example of an orthotropic velocity model constructed from field surface seismic data.

Key words: multicomponent wide-azimuth seismic data, fracture characterization, multiple fracture sets, orthorhombic anisotropy

1 INTRODUCTION

Naturally fractured rocks are widely recognized as potential hydrocarbon-bearing formations. Perhaps this is why the 2004 Summer Research Workshop of the Society of Exploration Geophysics (SEG) and the European Association of Geoscientists and Engineers (EAGE) was held to determine the state of the art of seismic characterization of fractured reservoirs. The workshop demonstrated that current industry capabilities are limited to a single set of parallel, vertical cracks embedded in an otherwise isotropic host rock. For circular cracks, this arrangement leads to the effective horizontal trans-

verse isotropy (HTI) whose parameters can be estimated from seismic data. The papers presented at the workshop exploited HTI model and discussed various approaches to inferring the crack density, fracture orientation, and the type of fluid infill from such seismic signatures as normal-moveout (NMO) velocities (Berthet et al., 2004), amplitude-versus-offset (AVO) variations (del Monte et al., 2004; Gray and Todorovic-Marinic, 2004; Minsley et al., 2004; Todorovic-Marinic et al., 2004), and shear-wave splitting coefficients (Gaiser and Van Dok, 2004).

As all the above mentioned techniques are based on measuring the magnitude of azimuthal anisotropy for a selected seismic signature and translating it into the parameters of a single set of cracks, they are bound to produce misleading results in the presence of differently oriented fractures. Such arrangements of multiple fracture sets with different orientations are often identified in the borehole televiewer data, and have been observed at numerous outcrops throughout the globe. Given the ubiquity of multiple fracturing, the inadequacy of existing fracture-characterization technology might be explained by an inherent nonuniqueness in inverting the effective anisotropy (estimated from seismic data) for the parameters associated with multiple crack systems. Indeed, the number of fracture-related parameters can be arbitrarily large whereas the maximum number of independent effective stiffness coefficients for any homogeneous rock volume is only 21. While the number 21 obviously imposes an ultimate limit on the number N of fracture sets that can be uniquely resolved from long-wavelength seismic data, this N is typically greater than one. Grechka and Tsvankin (2003) used the linear slip theory of Schoenberg (1980) to derive limits for N. They found, in agreement with the earlier results of Bakulin et al. (2000), that seismic data can uniquely constrain the parameters of up to two vertical, rotationally-invariant fracture sets embedded in isotropic background rock.

To make further progress in fracture characterization, one has to rely on certain microstructural information related to the cracks. Such information was utilized in the effective media theory proposed by Kachanov (1980). Being similar to Schoenberg's (1980) linear slip theory for dry cracks, Kachanov's theory adds the following important insight: the collective contribution of multiple sets of dry fractures to the effective elasticity is largely controlled by a symmetric, second-rank crack-density tensor. [Schoenberg and Sayers (1995) call such fractures "scalar."] The ability of representing multiple crack systems by a *second-rank* tensor leads to *orthotropic* effective symmetry for *any* orientation distribution of fractures and implies that arbitrarily oriented, vertical cracks can be replaced by *two* mutually *orthogonal* fracture sets (called the principal ones) as far as propagation of low-frequency seismic waves is concerned. Moreover, the effective orthotropy induced by dry cracks residing in a purely isotropic host rock turns out to be remarkably simple: it is fully described by only four independent quantities instead of nine needed for general orthotropy. These quantities are the two principal crack densities, e_1 and e_2, and the Lamé constants of the isotropic background, λ_b and μ_b.

The findings of Kachanov (1980; also review 1993) are extremely valuable for fracture characterization because they reduce any number of vertical fracture sets to just two and, thus, provide a theoretical basis for estimating parameters of multiple systems of fractures. Prior to using these theoretical predictions for such a parameter estimation, however, it is important to establish their accuracy and the range of applicability. This work has been done by Grechka and Kachanov (2006a; 2006b) and Grechka et al. (2006), who performed finite element simulations of the effective elasticity for a wide variety of crack arrays that contained planar, open and partially closed, intersecting and non-intersecting, circular and irregular dry fractures. These papers demonstrate that the deviations from effective orthotropy never exceed 2% in the entire range of the crack densities expected in naturally fractured formations. Moreover, the results of Grechka and Kachanov (2006a) indicate that the effective orthotropy holds for liquid-filled cracks even with a better accuracy due to the stiffening of fractures by fluids and a subsequent reduction of crack contribution to the overall elasticity. Following numerical verification of the effective crack-induced orthotropy, Grechka and Kachanov (2006a) proposed a technique for characterization of multiple vertical fracture sets. Their method utilizes 3D, multiazimuth, multicomponent seismic reflection data and yields estimates of the orientations and crack densities of two principal fracture sets, the density-normalized Lamé constants of the background, and the so-called fluid factor that ranges from 0 for dry cracks to 1 for fractures filled with a stiff liquid. Bakulin et al. (2000) also proposed a method for characterizing two orthogonal crack sets in isotropic background. Because their approach is based on the linear-slip theory, seismic signatures are expressed in terms of the fracture weaknesses instead of microstructural parameters, such as crack densities and fluid infill. Since in this we follow the microstructural approach from Kachanov (1980), we will mostly refer to studies based on this approach. The work by Bakulin et al. (2000) provides comprehensive results in the context of the linear-slip approach. Grechka and Kachanov (2006a, 2006b)

also provide a thorough numerical comparison between these approaches.

Here we apply this fracture-characterization technique to a 3D, 9C, wide-azimuth data set acquired by the Reservoir Characterization Project (Colorado School of Mines) over the tight-gas Rulison Field located in Colorado. We invert the interval NMO ellipses of P, S_1 (fast shear), and S_2 (slow shear) waves for the two principal crack densities, fracture azimuths, and fluid factors. The fracture orientations obtained from seismics are supported by direct borehole measurements, while the fluid factors turn out to be less than 0.01 as expected for the gas-bearing sandstones at Rulison. The theory also predicts almost elliptical anisotropy, and, indeed, we do not observe nonhyperbolic moveout on the P-wave long-spread data. Overall, the model of crack-induced orthotropy seems to adequately explain our data and allow us to characterize multiple fracture sets in the context of effective orthotropy for planar cracks (Kachanov, 1980, 1993; Grechka and Kachanov, 2006a, 2006b; Grechka et al., 2006).

2 THEORETICAL BACKGROUND

2.1 Effective anisotropy induced by vertical cracks

The model we assume here is based on a general representation of the effective compliance tensor, $\boldsymbol{s}_e$, of a rock containing cracks as a sum,

$$\boldsymbol{s}_e = \boldsymbol{s}_b + \Delta\boldsymbol{s}\,, \tag{1}$$

of the compliance, $\boldsymbol{s}_b$, of the isotropic unfractured background and the cumulative contribution, $\Delta\boldsymbol{s}$, of multiple fractures. In the non-interaction approximation (Kachanov, 1980; 1993; Grechka and Kachanov, 2006a), the nonzero elements of tensor $\Delta\boldsymbol{s}$ (in Voigt notation) are

$$\begin{aligned}
\Delta s_{11} &= \frac{16\,e_1\,(1-\nu_b^2)}{3\,E_b}\,(1-\varsigma)\,,\\
\Delta s_{22} &= \frac{16\,e_2\,(1-\nu_b^2)}{3\,E_b}\,(1-\varsigma)\,,\\
\Delta s_{44} &= \frac{32\,e_2\,(1-\nu_b^2)}{3\,E_b\,(2-\nu_b)}\,,\\
\Delta s_{55} &= \frac{32\,e_1\,(1-\nu_b^2)}{3\,E_b\,(2-\nu_b)}\,,\\
\Delta s_{66} &= \Delta s_{44} + \Delta s_{55}\,.
\end{aligned} \tag{2}$$

Here e_1 and e_2 are the densities of the two principal vertical fracture sets, $0 \le \varsigma \le 1$ is the fluid factor ($\varsigma \approx 0$ for dry cracks, $\varsigma \approx 1$ for liquid-filled ones), and E_b and ν_b are the Young's modulus and Poisson's ratio of the background, respectively. They are given by standard expressions,

$$E_b = \mu_b\,\frac{3\,\lambda_b + 2\,\mu_b}{\lambda_b + \mu_b} \quad \text{and} \quad \nu_b = \frac{\lambda_b}{2\,(\lambda_b + \mu_b)}\,, \tag{3}$$

in terms of the Lamé parameters λ_b and μ_b of the host rock. The compliance components (2) are written in the coordinate frame whose $\boldsymbol{x}_1$ and $\boldsymbol{x}_2$ axes are normal to the two principal fracture sets, and the $\boldsymbol{x}_3$ axis is vertical.

The predictions of the non-interaction effective media theory [equations (1) and (2)] appear to be remarkably simple. Yet, their high accuracy has been confirmed numerically for fracture arrays that grossly violate the assumptions of the non-interaction approximation (Grechka and Kachanov, 2006a; 2006b; Grechka et al., 2006). Specifically, formulations (1) and (2) remain sufficiently accurate for multiple sets of differently oriented, irregularly shaped, partially closed cracks that might intersect each other and form interconnected fracture networks. This means that long (compared to the crack sizes) seismic waves propagating through those fractures "see" them as if they were isolated and orthogonal to each other. As a result, the effective symmetry sensed by such long seismic waves is nearly orthorhombic even though no local symmetry exists on the scale of a few fractures. Hence, the effective crack densities and their orientations for a medium with many fracture sets reflect respectively, the compliance change induced by the presence of cracks and the corresponding principal crack directions. As a result, best-fit crack densities are approximately equivalent to projecting the actual crack densities corresponding to many different fracture sets onto the principal directions of the orthotropic effective elasticity tensor. Another conclusion that follows from equations (1) and (2) is that the effective anisotropy caused by dry fractures ($\varsigma \approx 0$) is almost elliptical (Kachanov, 1993; Grechka and Kachanov, 2006a). Below we show that seismic data acquired at Rulison support this theoretical result.

2.2 Inversion strategy

As follows from equations (1)–(3), the effective elastic properties of rocks with multiple vertical fracture sets are described by the parameter vector

$$\boldsymbol{M} = \{\lambda_b,\, \mu_b,\, e_1,\, e_2,\, \varsigma\} \tag{4}$$

that might vary spatially over the seismic survey area. Grechka and Kachanov (2006a) demonstrated that all components of $\boldsymbol{M}$ can be uniquely estimated from 3D, multiazimuth, multicomponent seismic reflection data. (Of course, seismic data constrain the density-normalized background Lamé constants rather than λ_b and μ_b themselves.) In

[b]

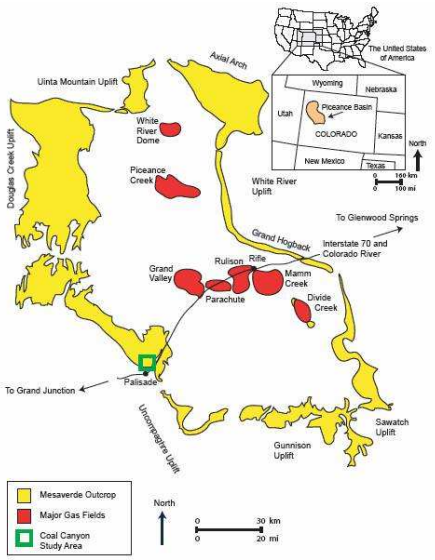

Figure 1. Map of gas-producing fields in Piceance Basin, Colorado (after Ellison, 2004).

particular, it has been shown that $\boldsymbol{M}$ can be unambiguously inverted from the data vector

$$\boldsymbol{D}(\boldsymbol{M}) = \left\{ \frac{V_{S1}}{V_{P0}}, \frac{V_{S2}}{V_{P0}}, \boldsymbol{W}^{P}, \boldsymbol{W}^{S1}, \boldsymbol{W}^{S2} \right\}, \quad (5)$$

where V_{P0}, V_{S1}, and V_{S2} are the velocities of vertically propagating P- and two split shear-waves (fast S_1 and slow S_2). The velocity ratios entering $\boldsymbol{D}$ can be computed from the zero-offset times after establishing the P-to-S event correspondence. The 2×2 matrices $\boldsymbol{W}$ in equation (5) are the normal-moveout (NMO) ellipses of pure modes reflected from a horizontal interface (Grechka and Tsvankin, 1998).

Vertical cracks result in effective orthorhombic media with two vertical symmetry planes, and since the reflector is horizontal, all three NMO ellipses $\boldsymbol{W}^{P}$, $\boldsymbol{W}^{S1}$, and $\boldsymbol{W}^{S2}$ are always co-oriented: their axes point along the normals to two principal fracture sets. Therefore, data vector (5) contains eight quantities: two velocity ratios and three pairs of the ellipse semi-axes, which are the symmetry-direction NMO velocities of P-, S_1-, and S_2-waves. Only seven quantities of those eight are generally independent because two out of four semi-axes of the shear-wave NMO ellipses coincide (Grechka et al., 1999). Thus, the functional dependence $\boldsymbol{D}(\boldsymbol{M})$ consists of seven equations and five unknowns. To aid understanding of this dependence, Appendix A gives the weak-anisotropy (or small-crack-density) approximations of both the elements of $\boldsymbol{D}$ and the anisotropic coefficients of orthorhombic media that were introduced by Tsvankin (1997).

In practice, we estimate data vectors (5) from wide-azimuth P, S_1, and S_2 common-midpoint (CMP) gathers. The NMO ellipses are obtained from 3D semblance analysis (Grechka and Tsvankin, 1999; Vasconcelos and Tsvankin, 2006) that maximizes the semblance by fitting an ellipse to the azimuthal variation of the NMO velocity. Another technique used in the industry is based on measuring the traveltime shifts of a given reflection event after azimuthally-independent NMO correction (Jenner, 2001). Once the azimuthal NMO analysis is completed, the Dix-type differentiation (Grechka and Tsvankin, 1999) is applied to calculate the interval NMO ellipses $\boldsymbol{W}^{P}_{\rm int}$, $\boldsymbol{W}^{S1}_{\rm int}$, and $\boldsymbol{W}^{S2}_{\rm int}$ and the interval data vector $\boldsymbol{D}_{\rm int}$. These ellipses typically exhibit some misalignments due a variety of factors (e.g., noise, possible azimuthal anisotropy of the host rock, reflector dip, fracture tilt, interaction of the closely spaced cracks) which are not captured in our model. The data indicate, however, that those misalignments are usually small (see Figure 9 and the corresponding discussion), therefore, we ignore them and estimate the parameter vector $\boldsymbol{M}$ at each CMP location though nonlinear minimization,

$$\mathcal{F} = \min_{(\boldsymbol{M})} ||\boldsymbol{D}_{\rm int} - \boldsymbol{D}(\boldsymbol{M})||\,, \quad (6)$$

that operates with the elliptical semi-axes only. In our inversion procedure, we use the exact expressions for $\boldsymbol{D}(\boldsymbol{M})$ rather than their small-crack-density approximations given in Appendix A.

Finally, we examine whether the inferred orthorhombic model correctly predicts seismic signatures that were not used in the inversion and compare our estimates of the crack densities and orientations with the available borehole measurements.

3 RULISON FIELD DATA

3.1 Brief overview of the field

Rulison Field, located in the South Piceance Basin, Garfield county, Colorado (Figure 1), produces gas from a 1,200 ft pay section of channel sand lenses stacked within the Cretaceous Mesaverde sandstone formation. Porosities (from 1% to 10%) and permeabilities (from 1 μD to 60 μD) of these sand bodies characterize the formation as a tight gas reservoir (Rojas, 2005). Because of such a low matrix permeability, it is believed (Johnson et al., 1987; Spencer, 1989; Lynn, 1999) that gas production is controlled by open natural fractures. Fracture orientations vary over the field area (Jansen, 2005), and their intersections are thought to be of importance for the reservoir production. The average thickness of sand lenses is about 10 ft, which makes them impossible to image with surface seismic data. Since neither sand bodies nor fracture zones can be

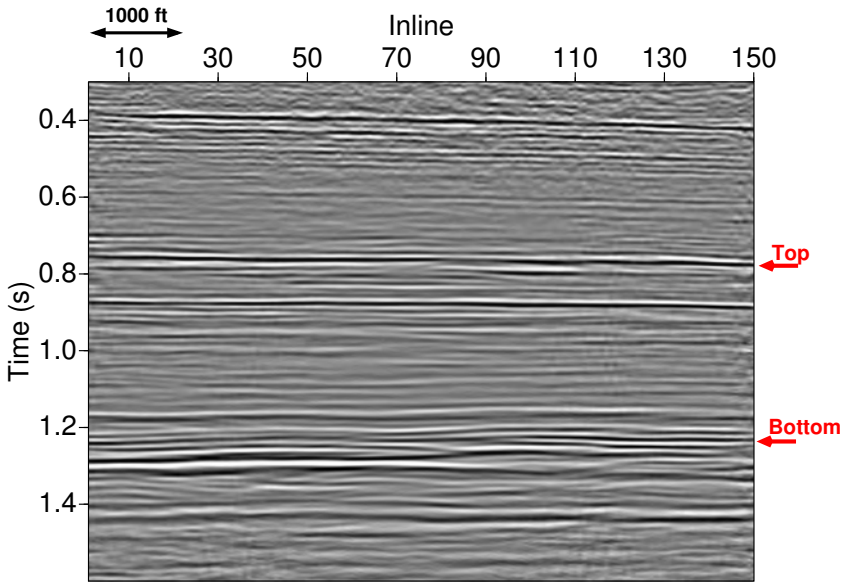

Figure 2. P-wave seismic section along Crossline 60. Arrows mark the reflection events used for azimuthal velocity analysis, which correspond the top and bottom of the reservoir.

individually isolated on seismic images, it is necessary to characterize the fractures collectively as an effective medium. Reflector dips at Rulison are small and can be neglected for the purposes of seismic data processing (Figure 2).

3.2 Data acquisition

A multicomponent seismic data set covering 5.5 km^2 was acquired by the Reservoir Characterization Project (Colorado School of Mines) in an effort to characterize Rulison Field with information from multiple sources (surface seismic, VSP, geomechanics, well logs, production data) and monitor the changes in production and stresses with time-lapse measurements. For our study, we use the baseline wide-azimuth, 3D, multicomponent seismic survey acquired with 3C vibrators and 3C geophones.

3.3 Data processing

Our input data consist of three CMP-sorted volumes (P, S_1 and S_2) corrected for the source-receiver statics and with source signature deconvolution applied. These pre-processing steps have been done by Veritas prior to our work. In addition, ground-roll suppression turned out to be necessary. Strong surface waves, present in all three data volumes, are particularly harmful for the shear reflections (Figure 3). As the S-wave events come later in time with the moveout slower than that of P-waves, a greater offset interval is covered by the ground-roll as opposed to P-data (compare Figures 3a and 3c). To suppress it, we resort our irregularly sampled (in offsets and azimuths) data into shot and receiver lines, where the sampling is regular, and apply an f-k_x-k_y filter that preserves the slopes up of 150 ms/kft. This approach to ground-roll suppression does not destroy azimuthal variations of traveltimes and results in a significant improvement of the reflected events (Figure 3).

Another pertinent issue concerns the two shear-wave volumes (S_1 and S_2) that we have at our disposal. The shear data have been rotated to the azimuth of the principal regional stress N45E. Treating this azimuth as the orientation of one of the principal fracture sets implies a constant fracture azimuth throughout the field, in contradiction with the laterally variable orientations of the P-wave NMO ellipses that we observe from the bottom of the producing interval. To mitigate this discrepancy, we rotated the shear volumes to the principal directions of these P-wave NMO ellipses at each CMP location prior to performing the S-wave velocity analysis. This is done because the model assumes shear-waves polarizations and NMO ellipses to be aligned. Because P-wave azimuthal anisotropy above the reservoir is small (the eccentricities of the P-wave NMO ellipses are consistently

smaller than 3%) we assume that the ellipse orientations are predominantly dictated by anisotropy at the reservoir level, so we use P-wave NMO ellipse orientations estimated from the bottom horizon events. Rotating shear-wave data in such manner will introduce errors in the estimated parameters wherever the model is inadequate.

After the ground-roll suppression and shear-wave rotation, we resort the data back to CMP geometry, create 9×9 (440×440 ft) superbins and extract the NMO ellipses over the survey area. At each superbin location, the NMO-ellipse estimation is performed for a window centered around the zero-offset times that correspond to the reservoir top and bottom horizons (Figure 2) interpreted from the P, S_1, and S_2 image volumes. The NMO ellipses are computed in 5 ms time increments over a window centered around the horizon times. The averaging lengths of the semblance windows are 35 ms for P- and 105 ms for shear-wave data. Our use of the interpreted horizons for velocity analysis ensures results that are consistent with the geologically-based time structure.

We obtain reliable (see Section 4.1) estimates of the P-waves NMO ellipses over the entire survey area (the corresponding semblance values range between 0.55 and 0.65). As the shear data are noisier (compare Figure 3b with 3d), the S-wave NMO ellipses have been estimated for only about one third of the survey area. We discarded the S-wave NMO ellipses whenever the semblances happened to be smaller than 0.25. Indeed, the reflection events cannot be visually distinguished on the gathers with such low semblance values. On the other hand, in the higher-quality data areas, the azimuthal traveltime variations are clearly seen on the gathers corrected with an azimuthally-constant NMO velocity (Figure 4).

After estimating the P, S_1, and S_2 NMO ellipses for the top and bottom horizons (located approximately at 4,000 ft and 7,500 ft depths) over the entire survey area, we proceed with the Dix-type differentiation (Grechka and Tsvankin, 1999) that yields the interval ellipses $\boldsymbol{W}^{P}_{\rm int}$, $\boldsymbol{W}^{S1}_{\rm int}$, and $\boldsymbol{W}^{S2}_{\rm int}$. Finally, minimizing the objective function (6), we invert $\boldsymbol{W}^{P}_{\rm int}$, $\boldsymbol{W}^{S1}_{\rm int}$, and $\boldsymbol{W}^{S2}_{\rm int}$ and the interval zero-offset time ratios for the fracture parameters.

3.4 Fracture characterisation

Figure 5 displays the inverted background velocity fields $V_{P,\,b}$ and $V_{S,\,b}$ [approximations (A9), (A10)] and the principal crack densities e_1 and e_2 (by definition, $e_1 \geq e_2$). The crack densities in Figure 5c are considerably greater than those in Figure 5d suggesting that the fracturing is dominated by the cracks trending in the WNW-ESE direction. Our results indicate that the western part of the area is controlled by a single fracture set that has density e_1, while the eastern part has a non-negligible contribution of other, differently oriented fractures that exhibit themselves as the set with crack density e_2 (Figures 5c and 5d). We also see that the areas of the highest crack densities do not necessarily coincide with the largest P-wave NMO ellipse eccentricities. We will revisit this issue below.

The background velocities (Figures 5a and 5b) show a sizeable contrast between the eastern and western portions of the study area, with both P- and S-wave velocities being slower in the west. The fluid factors ς have been estimated also but we do not display them because all the obtained values of ς are smaller than 0.01. These estimates are consistent with the fact that Rulison Field produces only gas.

3.5 Orthotropic model of the reservoir

The estimated background velocities and crack densities (along with the fluid factors $\varsigma \approx 0$) are sufficient for building an *orthorhombic* depth model of the reservoir. Figures 6 and 7 show the vertical velocities V_{P0} and V_{S0} and Tsvankin's (1997) anisotropic coefficients (the corresponding small-crack-density approximations can be found in Appendix A). We also display the anellipticity coefficients $\eta^{(1,\,2,\,3)}$ (right column in Figure 7) to demonstrate that the predicted anisotropy is nearly elliptical.

It is instructive to point out that the model in Figures 6 and 7 was obtained from reflection data only without using any borehole information to constrain the vertical depth scale. Although well-log or checkshot data are usually necessary for building orthorhombic subsurface models in depth domain (Grechka et al., 2005), we did not need such data in our study. The reason is that we explicitly targeted the *crack-induced* rather than general orthotropy. The former is significantly simpler because it is governed by fewer (five rather than nine) independent parameters. This reduction in the number of unknowns allowed us to rely solely on surface seismic data for building the unique orthorhombic model of Rulison reservoir. As Figures 6 and 7 indicate, the reservoir is noticeably anisotropic: the magnitudes of anisotropic coefficients $\epsilon^{(2)}$ and $\delta^{(2)}$ reach 0.2 at the highest total crack density $e = e_1 + e_2 = 0.17$ (Figures 5c and 5d).

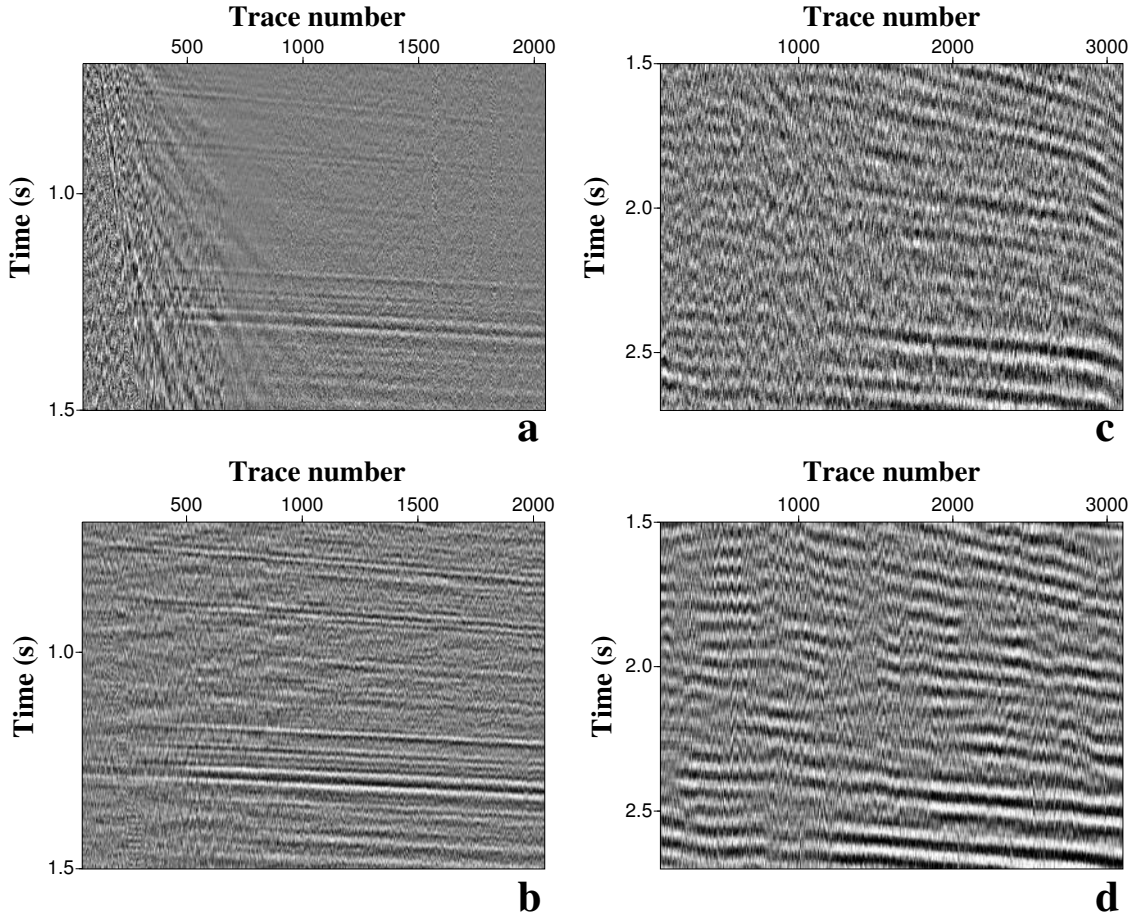

Figure 3. Representative input [(a) and (c)] and f-k_x-k_y-filtered [(b) and (d)] CMP gathers of P- (left column) and S_1-waves (right column). Offsets increase with increasing trace number. Both offsets and azimuths are irregularly sampled in the CMP domain.

3.6 Convention approaches to fracture characterization

Having estimated the reservoir parameters from both P- and S-wave data, we can predict what would happen if we relied S- or P-waves alone for fracture characterization. In a typical pure shear-wave survey, one would measure the shear-wave splitting coefficient, $\gamma^{(S)} \approx \gamma^{(1)} - \gamma^{(2)}$, and interpret it as the crack density of a single fracture set. The result of this interpretation (Figure 8a) suggests that the western part of the study area is more fractured than the eastern one, quite opposite to the conclusion drawn from Figures 5c and 5d.

If only P-wave data were used (e.g., Grechka and Tsvankin, 1999), one would estimate the eccentricity of the P-wave NMO ellipses, which is quantified by the difference of two δ coefficients, $\delta^{(1)} - \delta^{(2)}$. This difference, shown in Figure 8b, yields a similar result that the western part of the area is apparently more fractured than the eastern part.

The origin of these mutually contradictory conclusions can be understood from the approximations given by equations (A25) and (A26). Clearly, both quantities $\gamma^{(S)}$ and $\delta^{(1)} - \delta^{(2)}$ are proportional to the difference $e_1 - e_2$ between the crack densities of two principal fracture sets. As a consequence, the shear-wave splitting coefficients and the eccentricities of the P-wave NMO ellipses are useful for fracture characterization only if one fracture set dominates, that is, when $e_1 \gg e_2$. If multiple sets of cracks resulting in comparable e_1 and e_2 are present in the subsurface, both differences $\gamma^{(1)} - \gamma^{(2)}$ and $\delta^{(1)} - \delta^{(2)}$ become ambiguous. In particular, if the two principal crack densities coincide, $e_1 = e_2 \neq 0$, both differences vanish, $\gamma^{(1)} - \gamma^{(2)} = \delta^{(1)} - \delta^{(2)} = 0$, and one would arrive to an obviously incorrect conclusion that the fractures are absent.

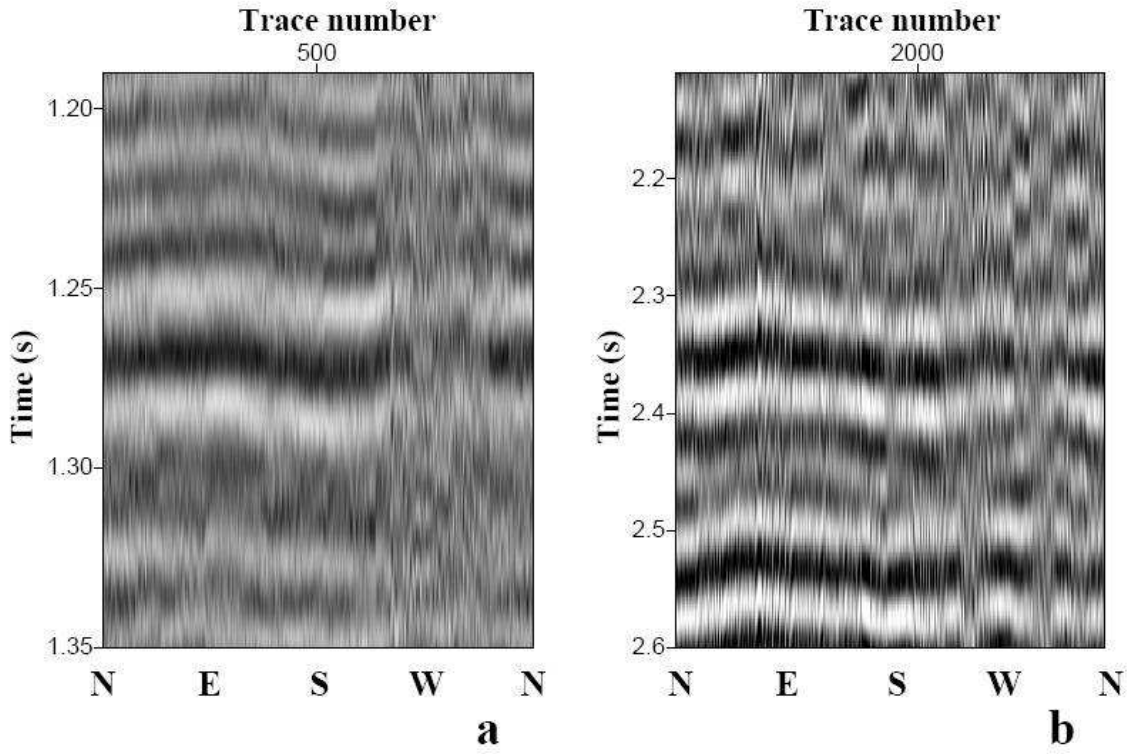

Figure 4. P- (a) and S_1-wave (b) gathers after azimuthally-invariant NMO correction. The traces are sorted by azimuth. The apparent cosine-type dependence of the residual moveout is indicative of azimuthal anisotropy. The reflection events at approximately at 1.27 s in (a) and at 2.35 s in (b) correspond to the reservoir bottom. The offset-to-depth ratios are between 0.8 and 1.0.

4 VERIFICATION OF RESULTS

An important part of any inversion procedure is assessing the errors in the estimated quantities. This section describes out efforts in this direction.

4.1 Variances in data and estimated parameters

We estimated the data variances associated with uncertainties in traveltime picking. A plausible picking interval was defined in accordance with the autocorrelation function of traces in a CMP gather. Specifically, we take this interval to be equal to the time lag where the autocorrelation drops by a factor of 10 from its zero-lag value. Such a definition yields the picking uncertainties equal to 8 ms for P- and 14 ms for S-waves. Next, a standard linear error-propagation technique is applied to translate these traveltime errors into uncertainties in the NMO ellipses. Finally, using the Fréchet-derivative matrix $\partial D_j/\partial M_i$, where M_i and D_j are the components of vectors $\boldsymbol{M}$ and $\boldsymbol{D}$ [equations (4) and (5)], we propagate the errors into the estimated quantities shown in Figure 5. This yields uncertainties of about 7% in the velocities $V_{P,b}$ and $V_{S,b}$ and 0.01 in the principal crack densities e_1 and e_2 within the 90% confidence interval.

Estimation of the model variances is not the only resource for validating our results. As we have already mentioned, the fluid factors ς turned out to be nearly zero at all CMP locations which is expected because of the absence of production of liquids (oil or water) at Rulison.

Another way of assessing the quality of our model assumptions is to analyze the misalignments in the orientations of the interval NMO ellipses for different wave modes. The histograms in Figure 9 exhibit pronounced peaks at 0° indicating that the ellipses are perfectly aligned at many CMP locations. Even though the presence of outliers (probably caused by noise in the data) makes the average differences in the ellipse orientations of P- and S_1-waves and P- and S_2-waves be equal to 12° and 17°, respectively, their significant portion can be attributed to fracture interaction or, in seismic terminology, to multiple scattering of elastic energy on the closely spaced cracks. For instance, Grechka

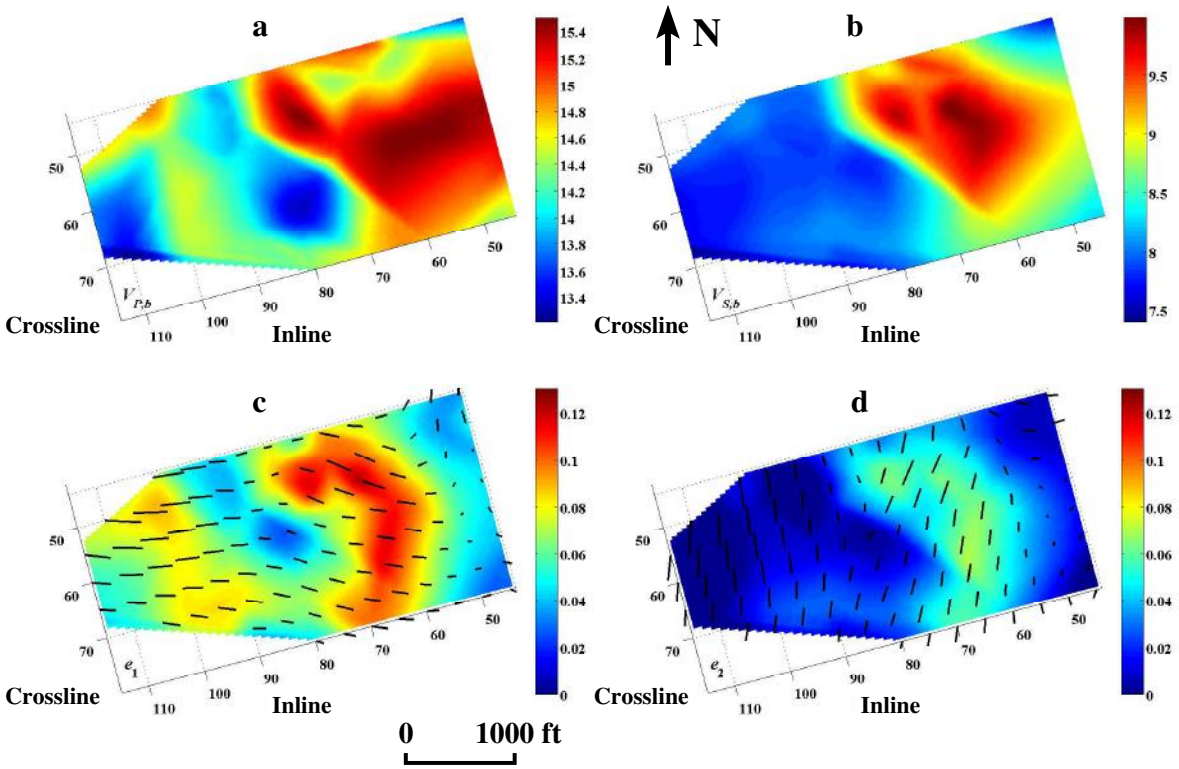

Figure 5. Output of fracture characterization: the background velocities $V_{P,\,b}$ and $V_{S,\,b}$ (in kft/s) of P- (a) and S-waves (b), and the principal crack densities e_1 (c) and e_2 (d). The directions of the principal fracture sets are shown with ticks. Their lengths are proportional to the eccentricities of the interval P-wave NMO ellipses (shown in Figure 8b).

and Kachanov (2006a) found this mechanism to be responsible for the NMO ellipse misalignments up to 12° at the total crack density $e = 0.14$. Thus, we conclude that orientations of the NMO ellipses are consistent with our fracture model over most of the survey area. In our parameter estimation procedure we do not take into account the distortions that might be introduced by the manner in which S-wave data was rotated.

4.2 Nonhyperbolic moveout

Our next step is to analyze the character of long-offset data in order to verify the ellipticity condition of the model of approximate effective orthotropy in isotropic background. Small values of the anellipticity coefficients η in the reservoir (right column of Figure 7) and nearly isotropic overburden imply the absence of nonhyperbolic moveout. Figure 10, which displays a typical long-spread P-wave gather, clearly supports this model conclusion. Indeed, no 'hockey-sticks' indicative of the nonhyperbolic moveout are observed in Rulison Field.

4.3 Borehole measurements

The survey area contains well B. RWF 542-20 (located at Inline 92, Crossline 76), where an FMI log was run and fractures in the entire reservoir were counted. Figure 11 compares the borehole fracture count with our estimate of the crack orientation. As a dominant set of cracks has been identified at Inline 92, Crossline 76 (Figures 5c and 5d), we do not display the second set in Figure 11 because it has nearly zero crack density. The fractures observed in FMI form two sets oriented approximately at N70W and N73E (blue in Figure 11). Clearly, these sets are not orthogonal to each other. And yet, our results suggest that their influence on propagation of long (compared to the fracture sizes) seismic waves is equivalent to that of two orthogonal sets. The dashed red line in Figure 11 shows the azimuth of the dominant equivalent set estimated from seismics.

Figure 11 can be regarded as an illustration of the resolution achievable from seismic data: while long seismic waves cannot resolve each individual fracture set, they are sensitive to the influence of all fractures simultaneously. This cumulative influ-

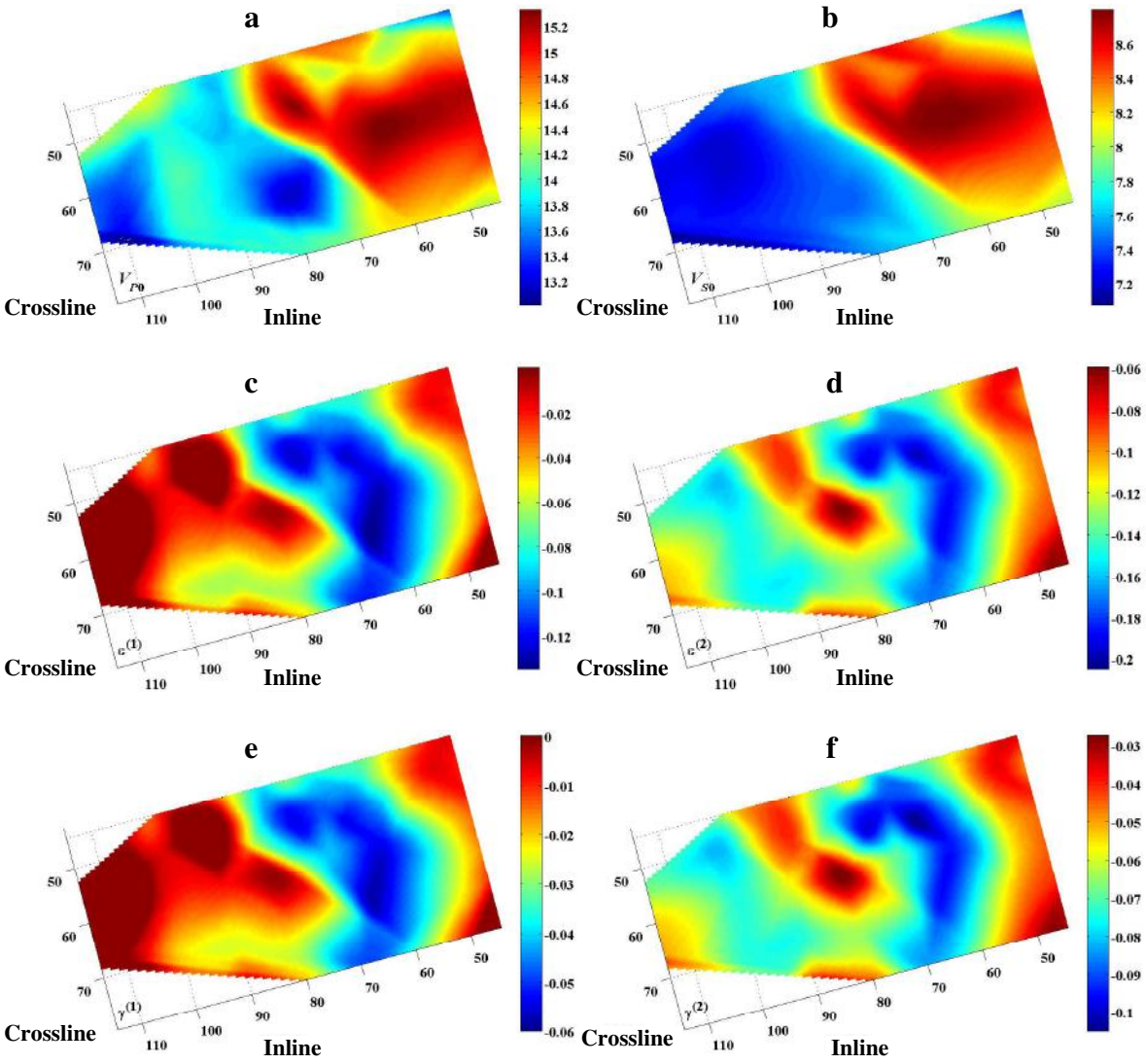

Figure 6. Vertical velocities V_{P0} and V_{S0} (in kft/s) and anisotropic coefficients $\epsilon^{(1,\,2)}$ and $\gamma^{(1,\,2)}$ at Rulison reservoir.

ence of all cracks on elastic wave propagation is described by the crack-density tensor (Kachanov 1980; Grechka and Kachanov, 2006a, their equation (2)) that can be represented in terms of contributions of mutually orthogonal (or principal) fracture sets. It is those principal sets that control the seismic signatures and, therefore, can be estimated from them. Thus, returning to Figure 11, we can state that our fracture-characterization results are consistent with the FMI log in well B. RWF 542-20.

4.4 Production data

There is a number of gas-producing wells drilled in Rulison Field, and, naturally, we attempted to establish a correlation between their Estimated Ultimate Recovery (EUR) and the obtained crack densities. As we observe no correlation, we would like to offer our thoughts on this issue because we feel that they might be relevant to other tight-gas fields.

First, the wells in Rulison Field have been drilled at different times in the past and, consequently, completed differently. Specifically, novel techniques of hydraulic fracturing and modern proppants significantly improved the gas recovery. Seismic data, however, are sensitive to both natural and man-made fractures and, obviously, do not allow us to separate a portion of the estimated crack densities primarily responsible for the production. Second, the EURs, being largely influenced by the completion techniques, vary rapidly throughout the field, whereas the crack densities

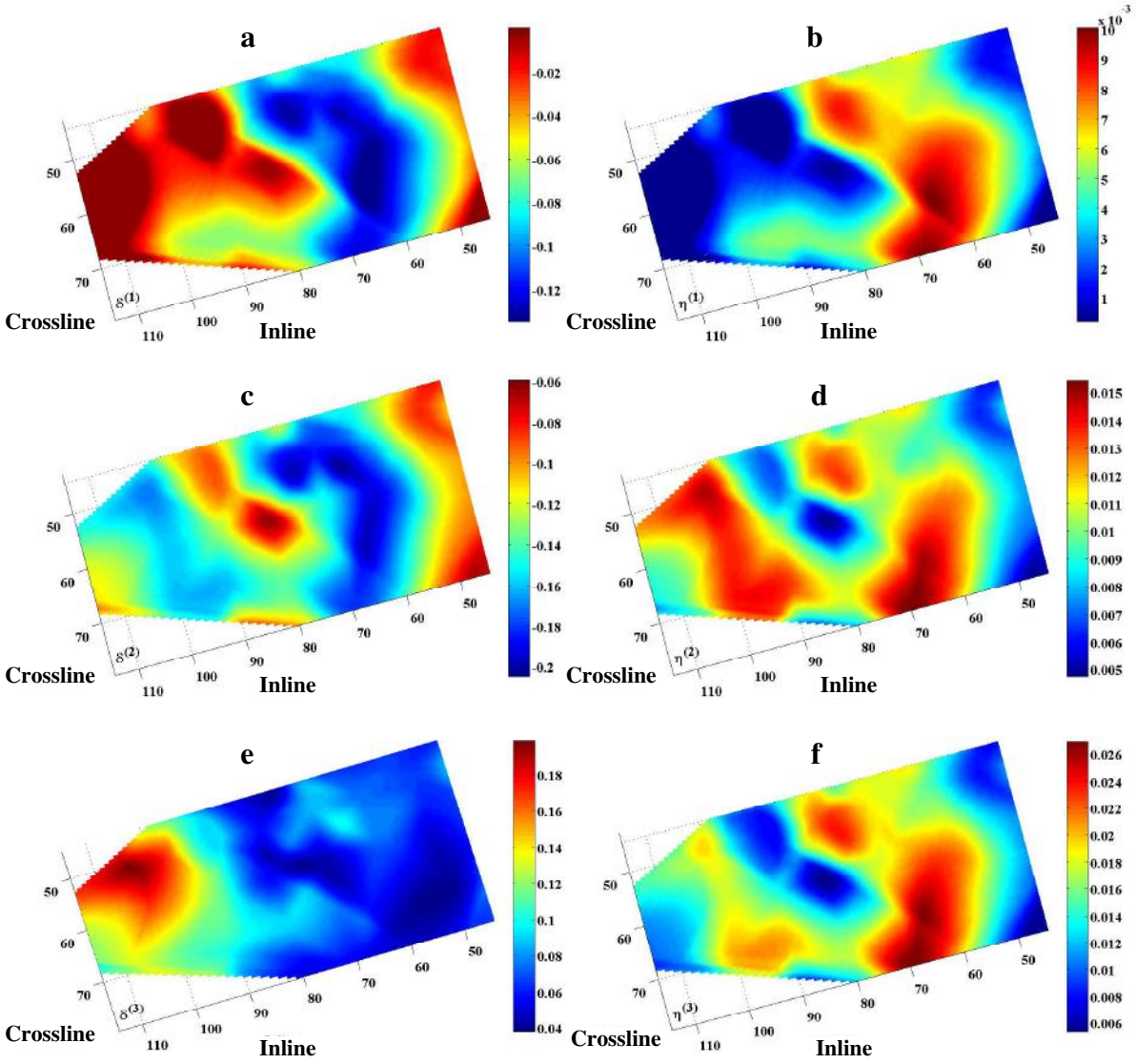

Figure 7. Anisotropic coefficients $\delta^{(1,\,2,\,3)}$ and $\eta^{(1,\,2,\,3)}$ at Rulison reservoir.

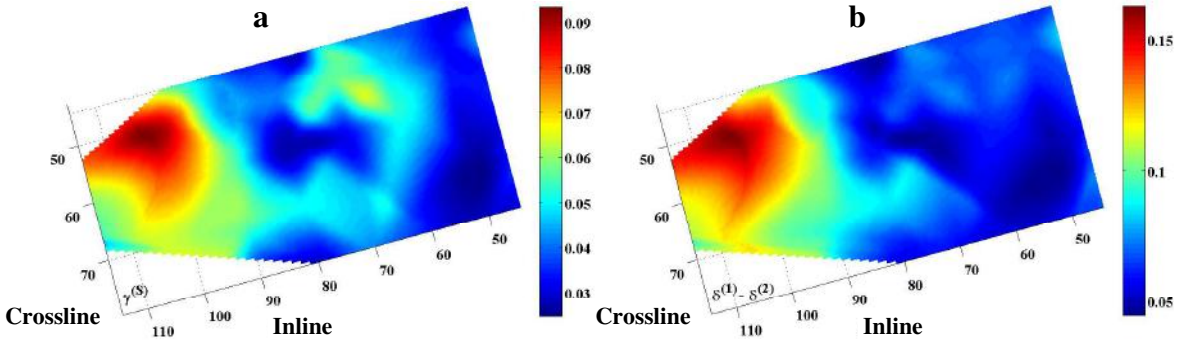

Figure 8. The shear-wave splitting coefficient $\gamma^{(\mathrm{S})}$ (a) and the eccentricity of the P-wave NMO ellipses $\delta^{(1)} - \delta^{(2)}$ (b) at Rulison reservoir.

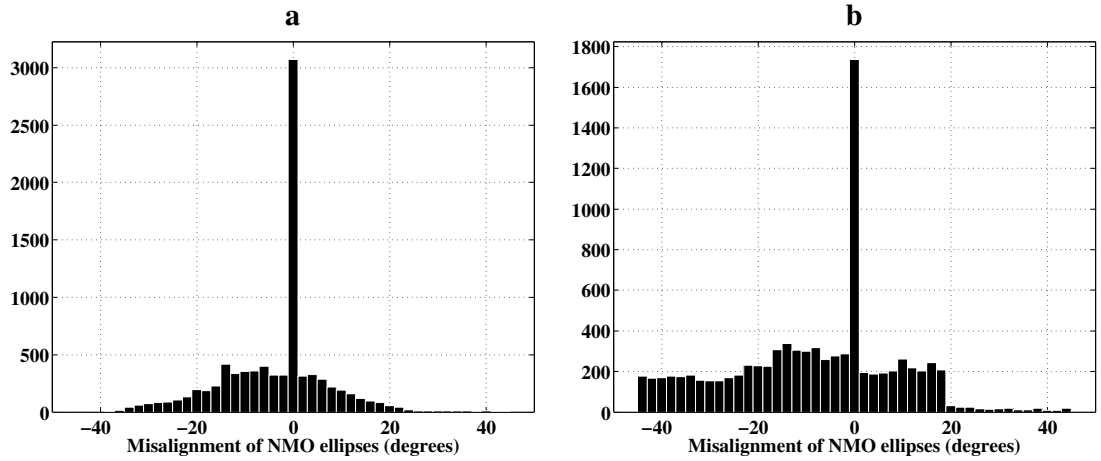

Figure 9. Histograms of azimuthal misalignments of the interval NMO ellipses of P- and S_1-waves (a) and P- and S_2-waves (b).

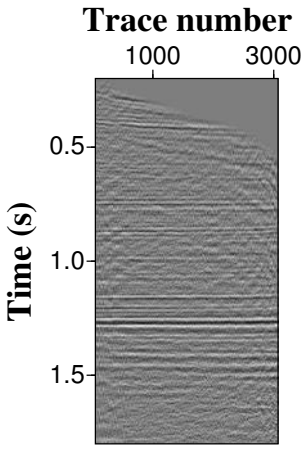

Figure 10. Typical long-spread P-wave gather after azimuthally-varying hyperbolic moveout correction. The offsets are irregularly sampled. Maximum offset-to-depth ratio is 2.0.

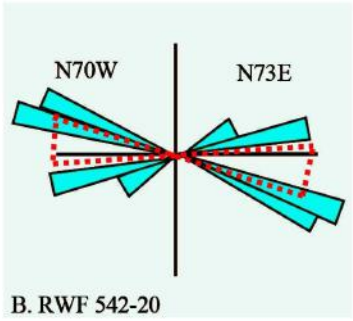

Figure 11. Fracture count (blue) in well B. RWF 542-20 located at Inline 92, Crossline 76 and the 90% confidence interval (dashed red) corresponding to the azimuth of the fracture set with density e_1 estimated from seismic data.

estimated from seismic data are relatively smooth (Figures 5c and 5d) given the lateral resolution of seismic data. This difference in the rate of change also hinders the correlation between the two.

The third and perhaps main reason for the absence of correlation can be sought in the physics of effective elasticity and permeability in low-porosity rocks. The quantity governing their overall elasticity is the crack density. Being the average of the cubed half-lengths of fractures, it carries no information about the crack widths or their openings. In contrast, the effective, crack-related permeability is essentially controlled by the fracture openings. Consequently, a short, wide-open crack (like the man-made ones) significantly contributes to the permeability and little to the elasticity. Thus, the effective permeability and elasticity are governed by different quantities that, in general, cannot be inferred from each other. However, with increasing pore space, an effective fractured porous medium is likely to show a direct cross-property relationship between its effective elasticity and permeability tensors. This cross-property connection would arise essentially from the microstructural interaction between cracks and pores.

5 DISCUSSION AND CONCLUSIONS

We have discussed seismic characterization of fractures at Rulison Field, Colorado. To the best of our knowledge, Rulison is the first case study where *multiple* fracture sets have been quantitatively characterized by not only their effective orientations but by their microstructural parameters:

two principal crack densities, type of infill, and background parameters. The key of our parameter-estimation methodology is the understanding (confirmed with extensive numerical modeling) that differently oriented, multiple vertical sets of cracks appear as two orthogonal sets for long seismic waves. Following this understanding, we have targeted the parameters of those two orthogonal (or principal) sets in our inversion. The obtained results point to the presence of fractures approximately aligned in the WNW-ESE direction in the western part of the study area. In contrast, at least two principal sets of cracks exist in its eastern part. Their crack densities reach $e_1 = 0.11$ and $e_2 = 0.06$ indicating that these fractures likely form an interconnected network. This follows from a straight forward geometrical consideration: it would be difficult to place many cracks corresponding to two sets of orthogonal fractures that have random locations and crack densities of $e_1 = 0.11$ and $e_2 = 0.06$ into a rock volume in a manner in which those fractures would not intersect each other. Thus, our inversion has identified places in the reservoir where swarms of intersecting cracks are likely to be present.

Under the assumption of approximate effective orthotropy in isotropic background (Kachanov, 1980; Grechka and Kachanov, 2006a, 2006b; Grechka et al., 2006), we have built an orthotropic depth model of the Rulison reservoir. The reconstructed orthorhombic velocity model explicitly attributes the observed anisotropy to the presence of fractures. This rock-physics constraint reduces the number of independent quantities to be estimated and obviously improves stability of the inversion. In particular, it allows the vertical P- and S-wave velocities and all anisotropic coefficients to be uniquely determined solely from 3D, multiazimuth, multicomponent seismic reflection data. We believe that Rulison is the first example of building a subsurface velocity model that has orthorhombic symmetry.

Special attention was paid in our study to verifying the obtained results. Here are the evidences that support our findings.

(1) We propagated uncertainties in the picked zero-offset times and NMO ellipses into the quantities that characterize the fractures. This yielded errors of about 7% in the P- and S-wave velocities in the host rock and around 0.01 in the principal crack densities.

(2) Rulison Field produces dry gas. While knowing this beforehand, we intentionally included the fluid factor into our unknowns. Its estimated values came out to be nearly zero in the entire study area, consistent with our information about of the type of fracture infill.

(3) The NMO ellipses of P-, S_1-, and S_2-waves recorded from horizontal reflectors are supposed to be co-oriented according to the adopted non-interaction theory of crack-induced anisotropy. In spite of the fact that we cannot account for errors induced by the rotation of shear-wave data, the ellipse misalignments observed in seismic data turned out to be comparable to those predicted by numerical modeling that takes into account interaction of closely spaced fractures.

(4) Anisotropy caused by multiple sets of dry cracks is almost elliptical. And, indeed, no nonhyperbolic moveout has been observed in the long-spread P-wave data.

(5) The available FMI log shows the fracture directions that are consistent with the effective principal crack orientations estimated from seismics.

Despite the above assurances that the obtained results not only exhibit internal consistency but also fit some independent external data, our estimates of the crack densities show little correlation with the EUR of wells in the field. While this poor correlation can be partially attributed to a variety of completion techniques used in the course of development of Rulison Field, we feel that its root cause is the physics of fluid flow through fractured media. For low-porosity (1% to 10%) sandstones at Rulison, fracture networks appear to provide the main pathways for the gas flow. The effective, crack-related permeability of these networks is essentially controlled by the fracture widths, whereas the seismic signatures are governed by the crack densities or the fracture lengths. If a relationship between the crack widths and lengths is absent, the effective permeability and elasticity are uncorrelated. Perhaps this is what seismic and production data at Rulison tell us. Still, even if this inference is correct, a more general question remains: under what geologic conditions does the crack density become a proxy for the permeability which would be useful for the reservoir development?

6 ACKNOWLEDGEMENTS

We thank the Reservoir Characterization Project (Colorado School of Mines) for providing seismic data and Shell E & P for permission to publish this paper. We are grateful to Jon Sheiman (Shell) for helping with data processing and Jorge Lopez (Shell) for his comments on the manuscript. The work described in our paper has been carried out during summer internship of I. V. at Shell E & P in 2005. We also thank Ilya Tsvankin and Rodrigo Fuck for their careful review of the manuscript and their enriching comments.

REFERENCES

Bakulin, A., V. Grechka, and I. Tsvankin, 2000, Estimation of fracture parameters from reflection seismic data. Part II: Fractured models with orthorhombic symmetry: Geophysics, **65**, 1803–1817.

Berthet, P., J.-P. Dunand, P. Julien, and J. Arnaud, 2004, 3D azimuthal velocity analysis on OBC data: *Summer Research Workshop, SEG/EAGE*, Vancouver, British Columbia, Canada.

del Monte, A. A., E. Angerer, C. Reiser, and C. Glass, 2004, Integrated approach for seismic fracture characterisation: *Summer Research Workshop, SEG/EAGE*, Vancouver, British Columbia, Canada.

Ellison, A. I., 2004, Numerical modeling of heterogeneity within a fluvial point-bar deposit using outcrop and lidar data: Williams Fork Formation, Piceance Basin, Colorado: MSc. thesis, University of Colorado.

Gaiser, J. E., and R. R. Van Dok, 2004, Multicomponent processing and fracture characterization analysis of two Wyoming 3-D PS-wave surveys: Pinedale Field and Washakie Basin: *Summer Research Workshop, SEG/EAGE*, Vancouver, British Columbia, Canada.

Gray, D., and D. Todorovic-Marinic, 2004, Fracture detection using 3D seismic: *Summer Research Workshop, SEG/EAGE*, Vancouver, British Columbia, Canada.

Grechka, V., and M. Kachanov, 2006a, Seismic characterization of multiple fracture sets: Does orthotropy suffice? *Geophysics*, in print.

Grechka, V., and M. Kachanov, 2006b, Effective elasticity of rocks with closely spaced and intersecting cracks: *Geophysics*, in print.

Grechka, V., A. Pech, and I. Tsvankin, 2005, Parameter estimation in orthorhombic media using multicomponent wide-azimuth reflection data: Geophysics, **70**, D1–D8.

Grechka, V., S. Theophanis, and I. Tsvankin, 1999, Joint inversion of P- and PS-waves in orthorhombic media: Theory and a physical-modeling study: Geophysics, **64**, 146–161.

Grechka, V., and I. Tsvankin, 1998, 3-D description of normal moveout in anisotropic media: Geophysics, **63**, 1079–1092.

Grechka, V., and I. Tsvankin, 1999, 3-D moveout inversion in azimuthally anisotropic media with lateral velocity variation: Theory and a case study: Geophysics, **64**, 1202–1218.

Grechka, V., and I. Tsvankin, 2003, Feasibility of seismic characterization of multiple fracture sets: Geophysics, **68**, 1399–1407.

Grechka, V., I. Vasconcelos, and M. Kachanov, 2006, The influence of crack shape on the effective elasticity of fractured rocks: *Geophysics*, submitted.

Jansen, K., Seismic investigation of wrench faulting and fracturing at Rulison Field, Colorado: MSc. thesis, Colorado School of Mines.

Jenner, E., 2001, Azimuthal anisotropy of 3-D compressional wave seismic data, Weyburn field, Saskatchewan, Canada, Ph.D. thesis, Colorado School of Mines.

Johnson, R. C., R. A. Crovelli, C. W. Spencer, and R. F. Mast, 1987, An assessment of gas resources in low-permeability sandstones of the Upper Cretaceous Mesaverde Group, Piceance Basin, Colorado: U.S. Geological Survey Open-File Report 87-357.

Kachanov, M., 1980, Continuum model of medium with cracks: Journal of the Engineering Mechanics Division, ASCE, **106** (EM5), 1039–1051.

Kachanov, M., 1993, Elastic solids with many cracks and related problems. In: Hutchinson, J. W., and T. Wu (Eds.), Advances in Applied Mechanics, **30**, 259–445.

Lynn, H. B., D. Campagna, K. M. Simon, and W. E. Beckham, 1999, Relationship of P-wave seismic attributes, azimuthal anisotropy, and commercial gas pay in 3-D P-wave multiazimuth data, Rulison Field, Piceance Basin, Colorado: Geophysics **64**, 1293–1311.

Minsley, B. J., M. E. Willis, M. Krasovec, D. R. Burns, and M. N. Toksöz, 2004, Investigation of a fractured reservoir using P-wave AVOA analysis: A case study of the Emilio Field with support from synthetic examples: *Summer Research Workshop, SEG/EAGE*, Vancouver, British Columbia, Canada.

Rojas, E., 2005, Elastic rock properties of tight gas sandstones for reservoir characterization at Rulison Field, Colorado: MSc. thesis, Colorado School of Mines.

Schoenberg, M., 1980, Elastic wave behavior across linear slip interfaces: J. Acoust. Soc. Am., **68**, 1516–1521.

Schoenberg, M., and C. Sayers, 1995, Seismic anisotropy of fractured rock: Geophysics, **60**, 204–211.

Spencer, C. W., 1989, Review of characteristics of low-permeability gas reservoirs in Western United States: American Association of Petroleum Geologists Bulletin, **73**, No. 5, 613–629.

Todorovic-Marinic, D., G. Larson, D. Gray, G. Soule, Y. Zheng, and J. Pelletier, 2004, Identifying vertical productive fractures in the Narraway gas field using the envelope of seismic anisotropy: *Summer Research Workshop, SEG/EAGE*, Vancouver, British Columbia, Canada.

Tsvankin, I., 1997, Anisotropic parameters and P-wave velocity for orthorhombic media: Geophysics, **62**, 1292–1309.

Vasconcelos, I., and I. Tsvankin, 2005, P-wave nonhyperbolic moveout inversion in azimuthally-anisotropic media: Methodology and real-data example: 67th Conference of EAGE, Madrid, Spain, Extended Abstracts.

APPENDIX A: SMALL-CRACK-DENSITY APPROXIMATIONS OF SEISMIC SIGNATURES

The goal of this Appendix is to develop an intuitive understanding of kinematic seismic signatures in formations containing multiple sets of vertical fractures. To arrive at tractable expressions, we assume that the principal crack densities are small, $\{e_1,\, e_2\} \ll 1$, and linearize all pertinent quantities in e_1 and e_2. As stated in the main text, arbitrarily oriented fractures embedded in an otherwise isotropic host rock cause nearly orthorhombic effective symmetry, therefore, Tsvankin's (1997) anisotropic coefficients introduced for orthorhombic media are of obvious importance for our study. We begin with deriving these anisotropic coefficients in terms of the governing parameters $\boldsymbol{M}$ [equation (4)] and then turn our attention to the NMO ellipses of pure modes reflected from horizontal interfaces.

A1 Anisotropic coefficients

As follows from equations (1)–(3), definition of the effective stiffness tensor, $\boldsymbol{c}_e = \boldsymbol{s}_e^{-1}$, and definitions (16)–(19), (23)–(26) of Tsvankin (1997), the vertical velocities V_{P0}, V_{S0} and relevant anisotropic coefficients, fully linearized in the crack densities, are:

$$V_{P0} = V_{P,\,b}\,\left[1 + \frac{2\,\lambda_b^2\,(\varsigma - 1)\,(e_1 + e_2)}{3\,\mu_b\,(\lambda_b + \mu_b)}\right], \tag{A1}$$

$$V_{S0} = V_{S,\,b}\left(1 - \frac{8}{3}\;e_1\,\frac{\lambda_b + 2\,\mu_b}{3\,\lambda_b + 4\,\mu_b}\right), \tag{A2}$$

$$\epsilon^{(2)} = \frac{8}{3}\;e_1\;(\varsigma - 1)\,, \tag{A3}$$

$$\epsilon^{(1)} = \frac{8}{3}\;e_2\;(\varsigma - 1)\,, \tag{A4}$$

$$\delta^{(2)} = \frac{8}{3}\;e_1\left[\frac{(\varsigma - 1)\;\lambda_b}{\lambda_b + \mu_b} - \frac{4\,\mu_b}{3\,\lambda_b + 4\,\mu_b}\right], \tag{A5}$$

$$\delta^{(1)} = \frac{8}{3}\;e_2\left[\frac{(\varsigma - 1)\;\lambda_b}{\lambda_b + \mu_b} - \frac{4\,\mu_b}{3\,\lambda_b + 4\,\mu_b}\right], \tag{A6}$$

$$\gamma^{(2)} = -\frac{8}{3}\;e_1\,\frac{\lambda_b + 2\,\mu_b}{3\,\lambda_b + 4\,\mu_b}\,, \tag{A7}$$

$$\gamma^{(1)} = -\frac{8}{3}\;e_2\,\frac{\lambda_b + 2\,\mu_b}{3\,\lambda_b + 4\,\mu_b}\,. \tag{A8}$$

Here

$$V_{P,\,b} = \sqrt{\frac{\lambda_b + 2\,\mu_b}{\rho}} \tag{A9}$$

and

$$V_{S,\,b} = \sqrt{\frac{\mu_b}{\rho}} \tag{A10}$$

are the velocities in the isotropic unfractured rock, ρ is the density, and the quantities λ_b, μ_b, e_1, e_2, and ς are described in the main text. Note that the anisotropic coefficients $\epsilon^{(2)}$, $\delta^{(2)}$, and $\gamma^{(2)}$, defined in the plane $[\boldsymbol{x}_1,\, \boldsymbol{x}_3]$ that contains the normal to the first fracture set with the crack density e_1, are proportional to e_1 and independent of e_2. Similarly, the coefficients $\epsilon^{(1)}$, $\delta^{(1)}$, and $\gamma^{(1)}$ are controlled by e_2 only. The same observations were made earlier by Bakulin et al. (2000).

A2 NMO ellipses and ratios of vertical velocities

Now we present the small-crack-density approximations for components of the data vector $\boldsymbol{D}$ [equation (5)]. The ratios of the vertical velocities are

$$\frac{V_{S1}}{V_{P0}} = \frac{V_{S0}}{V_{P0}}\sqrt{\frac{1+2\,\gamma^{(1)}}{1+2\,\gamma^{(2)}}} = \frac{V_{S,\,b}}{V_{P,\,b}}\left\{1 - \frac{2}{3\,\mu_b\,(\lambda_b+\mu_b)}\left[\lambda_b^2\,(\varsigma-1)\,e_1 + \frac{(3\,\lambda_b+2\,\mu_b)\,(\lambda_b^2\,\varsigma+4\,\mu_b^2) - \lambda_b^2\,(3\,\lambda_b-2\,\mu_b\,\varsigma)}{3\,\lambda_b+4\,\mu_b}\,e_2\right]\right\} \tag{A11}$$

and

$$\frac{V_{S2}}{V_{P0}} = \frac{V_{S0}}{V_{P0}} = \frac{V_{S,\,b}}{V_{P,\,b}}\left\{1 - \frac{2}{3\,\mu_b\,(\lambda_b+\mu_b)}\left[\lambda_b^2\,(\varsigma-1)\,e_2 + \frac{(3\,\lambda_b+2\,\mu_b)\,(\lambda_b^2\,\varsigma+4\,\mu_b^2) - \lambda_b^2\,(3\,\lambda_b-2\,\mu_b\,\varsigma)}{3\,\lambda_b+4\,\mu_b}\,e_1\right]\right\}. \tag{A12}$$

The pure-mode NMO ellipses from a horizontal reflector beneath a homogeneous orthorhombic layer are given by (Grechka and Tsvankin, 1998)

$$\frac{1}{V^2_{Q,\,\mathrm{nmo}}(\phi)} = W_{Q,\,11}\,\cos^2\phi + W_{Q,\,22}\,\sin^2\phi = \frac{\cos^2\phi}{\left[V^{(1)}_{Q,\,\mathrm{nmo}}\right]^2} + \frac{\sin^2\phi}{\left[V^{(2)}_{Q,\,\mathrm{nmo}}\right]^2}\,. \tag{A13}$$

Here $Q = \mathrm{P}$, S_1, or S_2 is the wave type, ϕ is the azimuth measured from the normal to the first fracture set, $W_{Q,\,11}$ and $W_{Q,\,22}$ are the nonzero elements of 2×2 matrices $\boldsymbol{W}$ that describe general NMO ellipses, and $V^{(i)}_{Q,\,\mathrm{nmo}}$ are the symmetry-direction NMO velocities. These velocities are conveniently expressed in terms of the P- and S-wave vertical velocities and the anisotropic coefficients listed above (Grechka et al., 1999):

$$V^{(i)}_{P,\,\mathrm{nmo}} = V_{P0}\,\sqrt{1\,+\,2\,\delta^{(i)}}\,, \quad (i=1,\,2)\,, \tag{A14}$$

$$V^{(1)}_{S1,\,\mathrm{nmo}} = V_{S1}\,\sqrt{1+2\,\sigma^{(1)}}\,, \tag{A15}$$

$$V^{(2)}_{S1,\,\mathrm{nmo}} = V^{(1)}_{S2,\,\mathrm{nmo}} = V_{S1}\,\sqrt{1+2\,\gamma^{(2)}} = V_{S2}\,\sqrt{1+2\,\gamma^{(1)}}\,, \tag{A16}$$

$$V^{(2)}_{S2,\,\mathrm{nmo}} = V_{S2}\,\sqrt{1+2\,\sigma^{(2)}}\,, \tag{A17}$$

where

$$\sigma^{(1)} = \left(\frac{V_{P0}}{V_{S1}}\right)^2(\epsilon^{(1)} - \delta^{(1)})\,, \tag{A18}$$

$$\sigma^{(2)} = \left(\frac{V_{P0}}{V_{S2}}\right)^2(\epsilon^{(2)} - \delta^{(2)})\,. \tag{A19}$$

Substitution of equations (A1)–(A10) into equations (A14)–(A19) and subsequent linearization yields

$$V^{(1)}_{P,\,\mathrm{nmo}} = V_{P,\,b}\left\{1 + \frac{2}{3\,\mu_b\,(\lambda_b+\mu_b)}\left[\lambda_b^2\,(\varsigma-1)\,e_1 + \frac{1}{3\,\lambda_b+4\,\mu_b}\left(3\,\lambda_b^3\,(\varsigma-1) + 16\,\mu_b\,\left(\lambda_b^2\,(\varsigma-1) + \lambda_b\,\mu_b\,(\varsigma-2) - \mu_b^2\right)\right)e_2\right]\right\}, \tag{A20}$$

$$V^{(2)}_{P,\,\mathrm{nmo}} = V_{P,\,b}\left\{1 + \frac{2}{3\,\mu_b\,(\lambda_b+\mu_b)}\left[\lambda_b^2\,(\varsigma-1)\,e_2 + \frac{1}{3\,\lambda_b+4\,\mu_b}\left(3\,\lambda_b^3\,(\varsigma-1) + 16\,\mu_b\,\left(\lambda_b^2\,(\varsigma-1) + \lambda_b\,\mu_b\,(\varsigma-2) - \mu_b^2\right)\right)e_1\right]\right\}, \tag{A21}$$

$$V^{(1)}_{S1,\,\mathrm{nmo}} = V_{S,\,b}\,\left\{1+\frac{8\,(\lambda_b+2\,\mu_b)}{3\,(\lambda_b+\mu_b)}\;e_2\,\left[\varsigma-\frac{\mu_b}{3\,\lambda_b+4\,\mu_b}\right]\right\}, \tag{A22}$$

$$V^{(2)}_{S1,\,\mathrm{nmo}} = V^{(1)}_{S2,\,\mathrm{nmo}} = V_{S,\,b}\,\left[1-\frac{8\,(\lambda_b+2\,\mu_b)}{3\,(3\,\lambda_b+4\,\mu_b)}\;(e_1+e_2)\right], \tag{A23}$$

$$V^{(2)}_{S2,\,\mathrm{nmo}} = V_{S,\,b}\,\left\{1+\frac{8\,(\lambda_b+2\,\mu_b)}{3\,(\lambda_b+\mu_b)}\;e_1\,\left[\varsigma-\frac{\mu_b}{3\,\lambda_b+4\,\mu_b}\right]\right\}. \tag{A24}$$

It is a simple matter now to construct the Fréchet-derivative matrix, $\boldsymbol{F}$, of the quantities given by equations (A11), (A12), (A20)–(A24) with respect to the elements of parameter vector $\boldsymbol{M}$ [equation (4)] and verify that all singular values of $\boldsymbol{F}$ are nonzero.

A3 Shear-wave splitting coefficient and the eccentricity of the P-wave NMO ellipse

Finally, we use the already derived approximations to demonstrate that such well-known fracture indicators as the shear-wave splitting coefficient and the eccentricity of P-wave NMO ellipse are controlled by the *difference* of two principal crack densities, e_1-e_2, and, therefore, insufficient for characterization of multiple fracture sets.

The eccentricity (or normalized elongation) of the P-wave NMO ellipse is just the difference of two δ coefficients. As follows from equations (A5) and (A6), the eccentricity is

$$\delta^{(1)}-\delta^{(2)} = \frac{8}{3}\;(e_1-e_2)\left[\frac{(1-\varsigma)\;\lambda_b}{\lambda_b+\mu_b}+\frac{4\,\mu_b}{3\,\lambda_b+4\,\mu_b}\right]. \tag{A25}$$

Similarly, definition of the shear-wave splitting coefficient, $\gamma^{(\mathrm{S})}\approx\gamma^{(1)}-\gamma^{(2)}$, and equations (A7), (A8) yield

$$\gamma^{(\mathrm{S})} = \frac{8}{3}\;(e_1-e_2)\;\frac{\lambda_b+2\,\mu_b}{3\,\lambda_b+4\,\mu_b}\,. \tag{A26}$$

Clearly, these signatures unambiguously constrain the crack density only for a single fracture set, that is, when one of the principal crack densities is zero.